Biomedical Optics EXPRESS

Prostate cancer detection using combined auto-fluorescence and light reflectance spectroscopy: *ex vivo study of human prostates*

Vikrant Sharma,[1,2] Ephrem O. Olweny,[3] Payal Kapur,[4] Jeffrey A. Cadeddu,[3] Claus G. Roehrborn,[3] and Hanli Liu[1,2,*]

[1] *Department of Bioengineering, University of Texas at Arlington, Arlington, TX 76019, USA*
[2] *Joint Program of Biomedical Engineering between University of Texas at Arlington and University of Texas Southwestern Medical Center at Dallas, Arlington, TX 76019, USA*
[3] *Department of Urology, University of Texas Southwestern Medical Center, Dallas, TX 75390, USA*
[4] *Department of Pathology, University of Texas Southwestern Medical Center, Dallas, TX 75390, USA*
**hanli@uta.edu*

Abstract: This study was conducted to evaluate the capability of detecting prostate cancer (PCa) using auto-fluorescence lifetime spectroscopy (AFLS) and light reflectance spectroscopy (LRS). AFLS used excitation at 447 nm with four emission wavelengths (532, 562, 632, and 684 nm), where their lifetimes and weights were analyzed using a double exponent model. LRS was measured between 500 and 840 nm and analyzed by a quantitative model to determine hemoglobin concentrations and light scattering. Both AFLS and LRS were taken on n = 724 distinct locations from both prostate capsular (n_c = 185) and parenchymal (n_p = 539) tissues, including PCa tissue, benign peripheral zone tissue and benign prostatic hyperplasia (BPH), of fresh *ex vivo* radical prostatectomy specimens from 37 patients with high volume, intermediate-to-high-grade PCa (Gleason score, GS ≥7). AFLS and LRS parameters from parenchymal tissues were analyzed for statistical testing and classification. A feature selection algorithm based on multinomial logistic regression was implemented to identify critical parameters in order to classify high-grade PCa tissue. The regression model was in turn used to classify PCa tissue at the individual aggressive level of GS = 7,8,9. Receiver operating characteristic curves were generated and used to determine classification accuracy for each tissue type. We show that our dual-modal technique resulted in accuracies of 87.9%, 90.1%, and 85.1% for PCa classification at GS = 7, 8, 9 within parenchymal tissues, and up to 91.1%, 91.9%, and 94.3% if capsular tissues were included for detection. Possible biochemical and physiological mechanisms causing signal differences in AFLS and LRS between PCa and benign tissues were also discussed.

OCIS codes: (170.1610) Clinical applications; (170.3650) Lifetime-based sensing; (170.6935) Tissue characterization; (170.4580) Optical diagnostics for medicine; (170.6510) Spectroscopy, tissue diagnostics.

References and links

1. O. Yossepowitch, A. Bjartell, J. A. Eastham, M. Graefen, B. D. Guillonneau, P. I. Karakiewicz, R. Montironi, and F. Montorsi, "Positive surgical margins in radical prostatectomy: outlining the problem and its long-term consequences," Eur. Urol. **55**(1), 87–99 (2009).
2. J. A. Wieder and M. S. Soloway, "Incidence, etiology, location, prevention and treatment of positive surgical margins after radical prostatectomy for prostate cancer," J. Urol. **160**(2), 299–315 (1998).
3. J. D. Sammon, Q. D. Trinh, S. Sukumar, P. Ravi, A. Friedman, M. Sun, J. Schmitges, C. Jeldres, W. Jeong, N. Mander, J. O. Peabody, P. I. Karakiewicz, and M. Harris, "Risk factors for biochemical recurrence following

#207541 - $15.00 USD Received 4 Mar 2014; revised 1 Apr 2014; accepted 7 Apr 2014; published 14 Apr 2014

radical perineal prostatectomy in a large contemporary series: A detailed assessment of margin extent and location," Urol. Oncol. **31**(8), 1470–1476 (2013).
4. A. Tewari and P. Narayan, "Novel staging tool for localized prostate cancer: a pilot study using genetic adaptive neural networks," J. Urol. **160**(2), 430–436 (1998).
5. L. W. D'Avolio, M. S. Litwin, S. O. Rogers, Jr., and A. A. Bui, "Automatic identification and classification of surgical margin status from pathology reports following prostate cancer surgery," AMIA Annu. Symp. Proc. **2007**, 160–164 (2007).
6. S. Salem, S. S. Chang, P. E. Clark, R. Davis, S. D. Herrell, Y. Kordan, M. L. Wills, S. B. Shappell, R. Baumgartner, S. Phillips, J. A. Smith, Jr., M. S. Cookson, and D. A. Barocas, "Comparative analysis of whole mount processing and systematic sampling of radical prostatectomy specimens: pathological outcomes and risk of biochemical recurrence," J. Urol. **184**(4), 1334–1340 (2010).
7. V. Iremashvili, S. D. Lokeshwar, M. S. Soloway, L. Pelaez, S. A. Umar, M. Manoharan, and M. Jordá, "Partial sampling of radical prostatectomy specimens: detection of positive margins and extraprostatic extension," Am. J. Surg. Pathol. **37**(2), 219–225 (2013).
8. H. Fukuhara, K. Inoue, H. Satake, K. Tamura, T. Karashima, I. Yamasaki, I. Tatsuo, A. Kurabayashi, M. Furihata, and T. Shuin, "Photodynamic diagnosis of positive margin during radical prostatectomy: preliminary experience with 5-aminolevulinic acid," Int. J. Urol. **18**(8), 585–591 (2011).
9. N. Lue, J. W. Kang, C. C. Yu, I. Barman, N. C. Dingari, M. S. Feld, R. R. Dasari, and M. Fitzmaurice, "Portable optical fiber probe-based spectroscopic scanner for rapid cancer diagnosis: a new tool for intraoperative margin assessment," PLoS ONE **7**(1), e30887 (2012).
10. B. Turkbey and P. L. Choyke, "Multiparametric MRI and prostate cancer diagnosis and risk stratification," Curr. Opin. Urol. **22**(4), 310–315 (2012).
11. V. Sharma, D. Kashyap, A. Mathker, S. Narvenkar, K. Bensalah, W. Kabbani, A. Tuncel, J. A. Cadeddu, and H. Liu, "Optical reflectance spectroscopy for detection of human prostate cancer," Conf. Proc. IEEE Eng. Med. Biol. Soc. **2009**, 118–121 (2009).
12. B. Kim, C. Temiyasathit, K. Bensalah, A. Tuncel, J. Cadeddu, W. Kabbani, V. Mathker, and H. Liu, "An efficient procedure for classification of prostate cancer in optical spectra," Expert Syst. Appl. **37**, 3863–3869 (2010).
13. G. Salomon, T. Hess, A. Erbersdobler, C. Eichelberg, S. Greschner, A. N. Sobchuk, A. K. Korolik, N. A. Nemkovich, J. Schreiber, M. Herms, M. Graefen, and H. Huland, "The feasibility of prostate cancer detection by triple spectroscopy," Eur. Urol. **55**(2), 376–384 (2009).
14. P. P. Dangle, K. K. Shah, B. Kaffenberger, and V. R. Patel, "The use of high resolution optical coherence tomography to evaluate robotic radical prostatectomy specimens," Int. Braz. J. Urol. **35**(3), 344–353 (2009).
15. L. Gao, H. Zhou, M. J. Thrall, F. Li, Y. Yang, Z. Wang, P. Luo, K. K. Wong, G. S. Palapattu, and S. T. Wong, "Label-free high-resolution imaging of prostate glands and cavernous nerves using coherent anti-Stokes Raman scattering microscopy," Biomed. Opt. Express **2**(4), 915–926 (2011).
16. Z. Jiang, D. Piao, G. Xu, J. W. Ritchey, G. R. Holyoak, K. E. Bartels, C. F. Bunting, G. Slobodov, and J. S. Krasinski, "Trans-rectal ultrasound-coupled near-infrared optical tomography of the prostate, part II: experimental demonstration," Opt. Express **16**(22), 17505–17520 (2008).
17. Z. Jiang, G. R. Holyoak, K. E. Bartels, J. W. Ritchey, G. Xu, C. F. Bunting, G. Slobodov, and D. Piao, "In vivo trans-rectal ultrasound-coupled optical tomography of a transmissible venereal tumor model in the canine pelvic canal," J. Biomed. Opt. **14**(3), 030506 (2009).
18. Z. Jiang, D. Piao, G. R. Holyoak, J. W. Ritchey, K. E. Bartels, G. Slobodov, C. F. Bunting, and J. S. Krasinski, "Trans-rectal ultrasound-coupled spectral optical tomography of total hemoglobin concentration enhances assessment of the laterality and progression of a transmissible venereal tumor in canine prostate," Urology **77**(1), 237–242 (2011).
19. V. C. Kavuri and H. Liu, "Hierarchical Clustering Method to Improve Transrectal Ultrasound-guided Diffuse Optical Tomography for Prostate Cancer Imaging," Acad. Radiol. **21**(2), 250–262 (2014).
20. R. J. Halter, A. R. Schned, J. A. Heaney, and A. Hartov, "Passive bioelectrical properties for assessing high- and low-grade prostate adenocarcinoma," Prostate **71**(16), 1759–1767 (2011).
21. V. Backman, M. B. Wallace, L. T. Perelman, J. T. Arendt, R. Gurjar, M. G. Müller, Q. Zhang, G. Zonios, E. Kline, J. A. McGilligan, S. Shapshay, T. Valdez, K. Badizadegan, J. M. Crawford, M. Fitzmaurice, S. Kabani, H. S. Levin, M. Seiler, R. R. Dasari, I. Itzkan, J. Van Dam, and M. S. Feld, "Detection of preinvasive cancer cells," Nature **406**(6791), 35–36 (2000).
22. D. Elson, J. Requejo-Isidro, I. Munro, F. Reavell, J. Siegel, K. Suhling, P. Tadrous, R. Benninger, P. Lanigan, J. McGinty, C. Talbot, B. Treanor, S. Webb, A. Sandison, A. Wallace, D. Davis, J. Lever, M. Neil, D. Phillips, G. Stamp, and P. French, "Time-domain fluorescence lifetime imaging applied to biological tissue," Photochem. Photobiol. Sci. **3**(8), 795–801 (2004).
23. P. Crow, N. Stone, C. A. Kendall, R. A. Persad, and M. P. Wright, "Optical diagnostics in urology: current applications and future prospects," BJU Int. **92**(4), 400–407 (2003).
24. V. Sharma, S. Shivalingaiah, Y. Peng, D. Euhus, Z. Gryczynski, and H. Liu, "Auto-fluorescence lifetime and light reflectance spectroscopy for breast cancer diagnosis: potential tools for intraoperative margin detection," Biomed. Opt. Express **3**(8), 1825–1840 (2012).

#207541 - $15.00 USD Received 4 Mar 2014; revised 1 Apr 2014; accepted 7 Apr 2014; published 14 Apr 2014

25. V. Sharma, J. W. He, S. Narvenkar, Y. B. Peng, and H. Liu, "Quantification of light reflectance spectroscopy and its application: determination of hemodynamics on the rat spinal cord and brain induced by electrical stimulation," Neuroimage **56**(3), 1316–1328 (2011).
26. R. Richards-Kortum and E. Sevick-Muraca, "Quantitative optical spectroscopy for tissue diagnosis," Annu. Rev. Phys. Chem. **47**(1), 555–606 (1996).
27. M. Y. Berezin and S. Achilefu, "Fluorescence lifetime measurements and biological imaging," Chem. Rev. **110**(5), 2641–2684 (2010).
28. G. A. Wagnières, W. M. Star, and B. C. Wilson, "In vivo fluorescence spectroscopy and imaging for oncological applications," Photochem. Photobiol. **68**(5), 603–632 (1998).
29. A. Bettelheim, H. Brown, K. Campbell, O. Farrell, and O. Torres, *Introduction to General, Organic and Biochemistry,* 10th ed. (Brooks/Cole, Cengage Learning, 2013).
30. G. Zonios and A. Dimou, "Light scattering spectroscopy of human skin in vivo," Opt. Express **17**(3), 1256–1267 (2009).
31. R. Nachabé, D. J. Evers, B. H. Hendriks, G. W. Lucassen, M. van der Voort, E. J. Rutgers, M. J. Peeters, J. A. Van der Hage, H. S. Oldenburg, J. Wesseling, and T. J. Ruers, "Diagnosis of breast cancer using diffuse optical spectroscopy from 500 to 1600 nm: comparison of classification methods," J. Biomed. Opt. **16**(8), 087010 (2011).
32. M. M. Shen and C. Abate-Shen, "Molecular genetics of prostate cancer: new prospects for old challenges," Genes Dev. **24**(18), 1967–2000 (2010).
33. D. A. Barron and D. R. Rowley, "The reactive stroma microenvironment and prostate cancer progression," Endocr. Relat. Cancer **19**(6), R187–R204 (2012).
34. T. Hastie, R. Tibshirani, and J. H. Friedman, *The Elements of Statistical Learning: Data Mining, Inference, and Prediction*, 2nd ed. (New York, Springer, 2009).
35. T. D. Wager, L. Y. Atlas, M. A. Lindquist, M. Roy, C.-W. Woo, and E. Kross, "An fMRI-Based Neurologic Signature of Physical Pain," N. Engl. J. Med. **368**(15), 1388–1397 (2013).

1. Introduction

Improved capabilities for prostate cancer (PCa) detection during diagnosis and treatment would be highly beneficial to both urologists and patients, with potential applications in surgical margin assessment during radical prostatectomy and cancer monitoring during active surveillance. The former is particularly important considering that in a recent comprehensive review, positive surgical margins (PSM) during radical prostatectomy (RP) were noted to be present in up to 38% of cases [1]. While the clinical significance of PSM is variable, largely depending on margin extent and location, PSM is generally considered an adverse factor for disease-free survival [2,3]. Thus, minimizing PSM during RP will lead to a lower risk of biochemical recurrence and reduction of further therapeutic treatments. While much effort has been made in the field of pathological analysis [4–7] to improve the detection accuracy of PSM and extraprostatic extension, there have been very few technical reports [8] on development of optical techniques to detect PSM *in vivo* during RP or *ex vivo* right after retrieval of the excised prostate specimens. Very recently, Lue et al. have reported a portable optical fiber probe-based spectroscopic scanner for rapid cancer diagnosis [9]. While it is possible that such a scanner has the potential to become a clinical platform for intraoperative margin assessment, it is unknown whether optical signatures of PCa tissue are distinct enough to be differentiated from adjacent non-cancer tissues.

The second major issue in prostate cancer management is detection of early-stage biologically aggressive disease. Prostate specific antigen (PSA) screening has led to a significant rise in diagnosing the incidence of prostate cancer, which is currently diagnosed by transrectal ultrasound (TRUS)-guided prostate biopsy. Novel methods, such as multiparametric MRI, have demonstrated the potential for improved detection of high grade cancer and risk stratification in newly detected prostate cancers, but confirmatory biopsies are still required [10]. In addition, it is less likely or feasible to utilize MRI as a screening tool for detection of aggressive prostate cancer due to its complexity, availability, and cost, in comparison with a TRUS-guided, office-based, portable imaging device.

Several recent studies, including our own, have investigated the use of optical techniques for minimally invasive or non-invasive detection of PCa. As a simple, compact, and hand-held tool, optical reflectance spectroscopy was examined for optical signatures and feasible detection of PCa using *ex vivo* prostate specimens [11,12]. Salomon et al. [13] reported a

#207541 - $15.00 USD Received 4 Mar 2014; revised 1 Apr 2014; accepted 7 Apr 2014; published 14 Apr 2014

triple spectroscopy method in *ex vivo* prostate tissue with a sensitivity and specificity of 75% and 87.3%, respectively, for PCa detection. Dangle et al. explored the possibility of evaluating PCa tissue by high-resolution optical coherence tomography (OCT) [14], while Gao utilized a coherent anti-Stokes Raman scattering (CARS) microscope to image PCa tissue and cavernous nerves with cellular resolution [15]. From the non-invasive aspect, Jiang et al. demonstrated the feasibility to optically image PCa tissue and its surrounding vasculature using diffuse optical tomography (DOT) based on laboratory phantom measurements [16] and animal studies [17,18]. Recently, Kavuri and Liu reported the feasibility of imaging human PCa tissue by DOT without prior information on PCa locations using an optode geometry integrated with a transrectal ultrasound probe [19]. Furthermore, electrical impedance was also a possible bio-character to identify PCa. Halter et. al. [20] reported the use of electrical properties to differentiate PCa tissue from benign tissue, showing an area under curve (AUC) of 0.9 when discriminating between benign and malignant prostate tissue, 0.75 when discriminating between low and high grade cancer tissue.

In the present study, we developed and then evaluated a dual-modal optical device (*dMOD*), which incorporates dual measurements from auto-fluorescence lifetime spectroscopy (AFLS) and light reflectance spectroscopy (LRS) in a single fiber-optic probe of 1-mm diameter. LRS is sensitive to both tissue morphology and biochemical composition, while AFLS, on the other hand, captures the dynamic characteristics of endogenous fluorophores in the nanosecond range and is highly sensitive to the biochemical environment of the tissue. Each of these techniques has been successfully applied for identification of cancer tissue [21,22], but neither of them has been applied to human PCa diagnosis [23] nor studied as a combined technique for cancer detection. In principle, the vasculature, morphology and biochemical composition of PCa-bearing tissue are expected to differ from those of benign tissues; the differences are presumably more pronounced in higher grade and more advanced PCa tissue than slow-growing, less aggressive ones. Thus, we hypothesized in this study that LRS and AFLS, alone or in combination, could be able to detect and identify PCa at high grades.

Specifically, we performed dual-modal optical spectroscopic measurements from 37 *ex vivo* human prostate specimens right after radical prostatectomy. Measurements from twenty nine ($n_p = 29$) out of the 37 glands were obtained from prostate parenchyma (i.e. tissue within the prostate capsules) and were used for characterization and classification of high grade PCa with Gleason score (GS) ≥7. Measurements from the rest of the prostate specimens ($n_c = 8$) were taken from capsular and extra capsular tissues. By the end of this study, we demonstrated that the *dMOD* is able to (1) discriminate high-grade PCa tissue (PCa) from benign peripheral zone prostate tissue (nPZ) and benign prostatic hyperplasia (BPH) in parenchymal tissues, and (2) result in excellent accuracy of above 90% in discriminating PCa from benign extra capsular tissues (ECT). In addition, several possible biochemical and physiological mechanisms were revealed and speculated to explain or interpret signal differences of AFLS/LRS induced by PCa. Overall, our results reported an excellent performance of this technique in its efficiency of detecting PCa at the individual Gleason grade from *ex vivo* human PCa-containing specimens.

2. Methods

2.1 Optical measurement setup and procedures

As reported earlier [24], the *dMOD* optical imaging system consisted of two modalities [Fig. 1(a)], namely AFLS and LRS, which were coupled through a custom-made fiber optic probe with 1-mm outer diameter (FiberTech Optica Inc., QC, Canada) [Fig. 1(b)], containing four fibers with different diameters [Fig. 1(c)]. The AFLS system consisted of a custom-made, single-channel, time correlated single photon counting system (ISS Inc., Champaign, IL)

#207541 - $15.00 USD Received 4 Mar 2014; revised 1 Apr 2014; accepted 7 Apr 2014; published 14 Apr 2014

machine and a pulsed supercontinuum laser source (5 ps, 20 MHz) (SC-450, Fianium Inc., Eugene, Oregon). This broadband laser light was filtered through a band pass filter at 447 nm with a bandwidth of 60 nm, as noted by 447 nm (60), and directed to the tissue sample for excitation. The auto-fluorescence signals and its corresponding lifetimes were measured using a photomultiplier tube (PMT) at four wavebands, namely, 532(10) nm, 562(40) nm, 632(24) nm, and 684(22) nm, each of which was selected sequentially through the emission filter wheel. Moreover, the LRS system consisted of a tungsten halogen light source (HL2000HP, Ocean Optics, FL), and a charged coupled device (CCD) array spectrometer (USB2000 + , Ocean Optics) that includes a spectral range of 500-840 nm, with a spectral sampling interval of 0.3 nm and a spectral resolution of 3 nm. More details on instrumentation is given in [24].

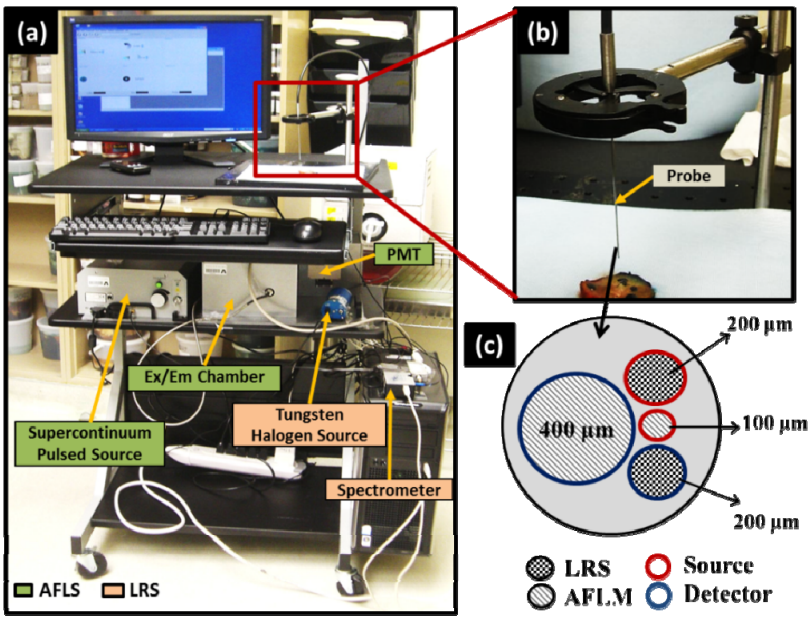

Fig. 1. Instrumentation: (a) Dual-modal optical system assembled on a portable cart for mobile capability to meet clinical needs; (b) close view of the optical probe positioned near the prostate specimen before actual optical readings; (c) front view of the probe showing arrangement of source and detector fibers for both AFLS and LRS.

2.2 Patients and surgical procedures

The study was conducted as per guidelines of the Institutional Review Board at the UT Southwestern Medical Center, Dallas, TX; each patient's informed consent was obtained before the surgery. Patients were selected with (a) an intermediate-to-high grade of disease (GS ≥ 7) and (b) a moderate-to-high volume of prostate cancer (at least two contiguous biopsy cores, each of which had 20% or more cancer involvement and/or bulky disease by endorectal MRI), so as to optimize spectral yield in this initial study. Each patient underwent robotic-assisted radical prostatectomy by one of two surgeons (JAC and CGR); then, the prostate glands were extracted after being disconnected from their blood supply for at least 30 minutes.

2.3 Experimental procedures

Resected prostate glands were immediately immersed in saline, and submitted for the dual-modal spectroscopy measurement [Fig. 2(a)]. For parenchymal tissue measurements, each of 29 glands ($n_p = 29$) was first inked on the capsule first, as per standard protocol at UTSW for histological evaluation (blue for the left lobe; orange for the right lobe) [Fig. 2(b)]. Dyes were

#207541 - $15.00 USD Received 4 Mar 2014; revised 1 Apr 2014; accepted 7 Apr 2014; published 14 Apr 2014

fixed using acetic acid washes so that the ink on the capsule would not be transferred into the parenchymal tissues. Then, the specimens were cut in a coronal plane through the location of possible tumor nodules as determined by pre-surgery biopsy mapping, pre-surgery MRI and/or palpation, such that tumor nodules were highly likely to be visible at the cut cross sections [Fig. 2(c)]. When the cancer tissue was not clearly identified by visual inspection, a Diff quick-stained touch-prep slide was made of suspected cancer-bearing tissue, confirming the location of PCa cells cytologically. The locations of nPZ and BPH regions on the cut surfaces of the specimens were also identified.

The dual-modal optical system [Fig. 1(a)] was then introduced to start the measurements. The *dMOD* probe [Figs. 1(b) and 1(c)] was placed just in contact with the cut surface of the prostate gland, without pressing the gland, and LRS and AFLS spectra were recorded from each of the pre-specified regions (PCa, nPZ, and BPH) [Fig. 2(d)]. Given the wavelength range used, we expect that AFLM would sense the tissue depth within 1 mm. For LRS, the fiber diameter and the source-detector separation employed would give rise to a best sensitivity at 1-2 mm depth. Thus, both of them interrogated ~1 mm tissue in depth. Also, since our AFLM/LRS measurement was point-based, eight repeated measurements from adjacent spots were obtained in each region (3-5 mm in diameter) for each type of tissues (i.e., prostate cancer, normal, and BPH) from each specimen to account for tissue heterogeneity.

After all the optical measurements were complete, each measured region was then marked with black ink, and a thin (~1 mm thick) section of each measured region was separately removed and submitted for histological evaluation [Fig. 2(e)]. Hematoxylin and eosin stained sections from these sets of submitted tissue were evaluated by a urologic pathologist to confirm the presence and extent of PCa and to determine the corresponding Gleason grade. Measured spectra were further categorized into different grade groups according to the histologically confirmed results.

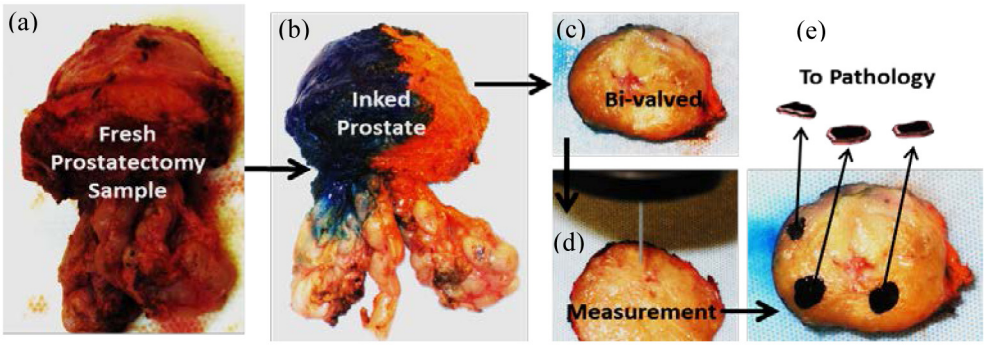

Fig. 2. Measurement Protocol: a freshly removed prostate specimen (a) was inked (b); then bi-valved in a coronal plane (c). After identifying benign peripheral zone tissue (nPZ), benign prostatic hyperplasia (BPH), and suspicious lesions for PCa, optical measurements were performed on the selected regions (d). Then, the measured regions were black-inked, removed, and sent for pathology confirmation (e), where black markings represent the removed tissue pieces that were optically measured and then sent for pathology analysis.

For capsular and/or extra-prostatic tissue measurements (n_c = 8) on the gland capsules, freshly resected samples were randomly selected for measurement. The measurement protocol was the same as the one used for parenchymal tissue measurements, except that the prostate glands were measured before inking. Three types of extra capsular tissues (ECT) were measured, namely, tissues at the prostate base near the bladder, urethra at the prostate apex, and prostate capsular tissues. For each prostate gland, 2-3 regions of each type were identified, and five dual-modal optical readings were taken on each region. Given eight prostate specimens, each of which had 3-5 regions measured at five times, we had a total of

#207541 - $15.00 USD Received 4 Mar 2014; revised 1 Apr 2014; accepted 7 Apr 2014; published 14 Apr 2014

185 locations measured. Then, each of the measured regions was submitted to pathology for analysis; all capsular tissues were confirmed to be benign after histopathology examination.

2.4 LRS and AFLS data processing for both PCa and benign tissues

A spectral width of 500-840 nm was chosen for data analysis; the corresponding data were fitted to a mathematical model [Eq. (1)], details of which have been described in [25].

$$R(\lambda) = \frac{\mu_s'(\lambda)}{k_1 + k_2 \mu_a(\lambda)}. \quad (1)$$

Briefly, $R(\lambda)$ is the measured spectral reflectance, which is associated with optical absorption and scattering coefficients (μ_a and μ_s') of the tissue by Eq. (1); k_1 and k_2 are instrument calibration constants. In principle, values of μ_a result mainly from a variety of chromophores in tissue such as oxygenated hemoglobin (HbO), deoxygenated hemoglobin (Hb), total hemoglobin (HbT), and β-carotene within the measured tissues. Also, values of μ_s' are closely related with cell size and density [25] and can be obtained at specific wavelengths. Thus, fitting Eq. (1) to the measured LRS data allowed us to obtain overall six LRS-based parameters including five fitted parameters (i.e., HbO, Hb, melanin, β-carotene, and light scattering coefficient at 750 nm) and one derived parameter (HbT = Hb + HbO) per measured spot. For parenchymal tissue analysis, the absorption spectra of the surface inking dyes were also incorporated in the model to account for any contamination from the dyes during the slicing of the prostate tissue. Furthermore, when we utilized only LRS parameters for statistical testing and tissue classification, statistical differences in fitted parameters for PCa, nPZ and BPH were analyzed using a linear mixed model regression analysis implemented in SAS (SAS Institute Inc., Cary, NC, USA).

For AFLS, four auto-fluorescence decay curves corresponding to four emission wavelengths (see Section 2.1) were obtained at each measured spot/location. These curves were first normalized and then used to fit a two-exponent model, as described by Eqs. (2a) and (2b).

$$I(t) = a_1 exp(-t/\tau_1) + a_2 exp(-t/\tau_2) + c \quad (2a)$$

$$\tau_m = (a_1\tau_1^2 + a_2\tau_2^2)/(a_1\tau_1 + a_2\tau_2), \quad (2b)$$

where τ_1 and τ_2 represent the lifetime of two auto-fluorescence decay components, a_1 and a_2 are their respective weights, and c is a baseline offset. The integral-intensity-weighted mean lifetime (τ_m) was also calculated for each curve [24]. Thus, we obtained five fitted features for each of the four emission wavelengths, giving us overall 20 parameters per measured location. As in case of LRS, each of these features was analyzed for statistical differences between PCa vs. nPZ, and PCa vs. BPH, using a linear mixed model regression analysis.

2.5 Classification and receiver operating characteristic (ROC) for parenchymal tissues

To examine the ability to discriminate PCa from benign tissue, two classification approaches were implemented. First, we tested the ability to differentiate prostate cancer (PCa, all grades combined) from benign nPZ and BPH using a 3-tissue-type classification model. Next, we evaluated the ability to differentiate individual grades of PCa with GS = 7, 8, 9 from benign nPZ and BPH using a 5-tissue-type classification model. These two classification approaches were evaluated for all three techniques, namely, LRS, AFLS, and *dMOD* (LRS + AFLS combined).

Specifically, we implemented a two-phase process for either 3-tissue-type or 5-tissue-type classification in order to effectively assess the classification accuracy for each technique. Phase one was to implement a feature selection algorithm so as to select a best feature set for cancer classification. In Section 2.4, we mentioned that fitting Eqs. (1), (2a) and (2b) to LRS

#207541 - $15.00 USD Received 4 Mar 2014; revised 1 Apr 2014; accepted 7 Apr 2014; published 14 Apr 2014

and AFLS data, respectively, would allow us to quantify multiple characteristic parameters or features (5 for LRS, 20 for AFLS, and thus 25 for *dMOD*), which could be utilized for PCa discrimination. However, all these features may not contribute equally and constructively to the classification model. An optimal feature set may allow better classification by reducing such problems as multicollinearity, redundancy, and overfitting of data. Thus, similar to our previous work [24], we employed sequential feature selection using a multinomial logistic regression model in this study. The actual determination of optimal features will be given in Section 3.1.

In phase two, for either 3-tissue-type or 5-tissue-type classification, we developed a multinomial logistic regression (MLR) model [24] along with 10-fold cross-validation [see Appendix] to classify respective types of prostate tissues and to obtain corresponding classification parameters for each tissue type. The procedures for this MLR-based classification are outlined in a flow-chart in Fig. 3, including (1) splitting data into 10 sub-groups; (2) using 90% of the data (*Tr*) for model training and 10% of the data (*Te*) for model testing; (3) generating an MLR-based classification model based on *Tr*; (4) generating ROC curves for each class of prostate tissues; (5) calculating the classification thresholds for PCa tissues; (6) testing the classification model derived from *Tr* with the independent data set, *Te,* by determining sensitivity (Sn), specificity (Sp), and accuracy (Acc); (7) performing ROC analysis based on MLR model and obtaining the area under curve (AUC) for each class of tissues; (8) repeating steps (2)-(7) 10 times using different sub-groups of *Tr* and *Te* for 10-fold cross validation and obtaining averaged Sn, Sp, Acc, and AUC; (9) repeating steps (1) - (8) 10 times after randomizing or regrouping the 10 sub-groups for *Tr* and *Te*, and thus achieving grand average values for means and standard deviation of Sn, Sp, Acc, and AUC. Note that the entire classification and ROC analysis were performed separately and independently for both 3-tissue-type and 5-tissue-type classification approaches.

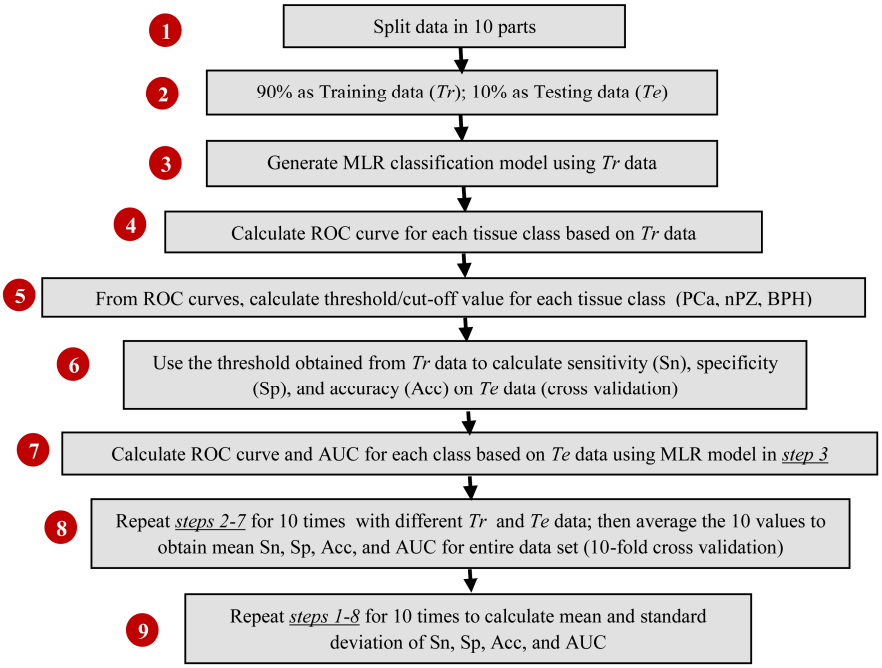

Fig. 3. A flow chart describing calculation of sensitivity, specificity, accuracy and generation of ROC curves through cross-validated classification process.

#207541 - $15.00 USD Received 4 Mar 2014; revised 1 Apr 2014; accepted 7 Apr 2014; published 14 Apr 2014

2.6 Data analysis for extracapsular tissues on the gland capsules

The data analysis procedures given in Sections 2.5 were used to analyze parenchymal tissues first; then they were repeated to investigate capsular and extra-capsular tissues. The same multinomial classification model with 10-fold cross validation was performed to evaluate the accuracy of *dMOD* to discriminate PCa from ECTs and nPZ. We again utilized 3-tissue-type and 5-tissue-type classification approaches to classify ECTs: the three tissue types included PCa, nPZ, and ECT; the five tissue types included PCa (GS 9), PCa (GS 8), PCa (GS 7), nPZ and ECT. Therefore, the 3-tissue-type classification method tested the accuracy in identifying any level of high grade PCa in presence of benign ECTs and nPZ tissue, whereas the 5-tissue-type classification tested the accuracy of differentiating specific high grade PCa at GS=7, 8, and 9 in the presence of benign ECTs and nPZ tissues.

3. Results

3.1 Results from prostate parenchymal tissues

A total of 29 patients were enrolled for this part of study (i.e., measurements from prostate parenchymal tissues); 6 out of 29 were excluded from the final analysis since their PCa tissues were made up only 25% or less over the entire tissue sampling evaluation, according to the final histology results. Mean (standard deviation) patient age was 60.7 (6.0) years. Several patients had multiple foci of PCa, resulting in 27 PCa regions, which were measured from 23 different prostate glands. As previously mentioned, 8 (or 9 from a few PCa regions) distinct spectral measurements were obtained from each region yielding a total of 221 PCa, 176 nPZ and 142 BPH measurements (see Table 1). Note that the numbers of measurements from nPZ and BPH reflect measurements from benign regions of the PCa-containing glands with the given GS.

Table 1. Number of measurements classified by tissue type*

	GS-7	GS-8	GS-9	Total
$N_{Subjects}$	13	4	6	**23**
$N_{Regions}$	15	5	7	**27**
N_{meas} **(PCa)**	125	40	56	**221**
N_{meas} **(nPZ)**	104	32	40	**176**
N_{meas} **(BPH)**	88	24	30	**142**

* For each Gleason column, the number of measurements for PCa is approximately equal to $N_{Regions} \times 8$, with a few cases having nine repeated measures in the selected regions.

Analysis of means for AFLS data revealed that integral-intensity-weighted mean lifetimes (τ_m) for PCa were significantly ($p < 0.05$) different from all other benign tissue types at all four wavelengths. While the lifetime of nPZ was shorter, BPH had a longer lifetime than PCa, consistently at all four wavelengths [Fig. 4(a)]. For LRS, analysis of means also showed statistical differences between PCa versus nPZ and PCa versus BPH for multiple fitted parameters [Fig. 4(b)]. Specifically, hemoglobin levels and β-carotene concentration were significantly smaller in PCa tissue than nPZ; BPH on the other hand showed significantly reduced deoxy-hemoglobin and β-carotene concentrations as compared to PCa tissue. One important observation is that light scattering was found significantly increased in PCa compared to all of the benign parenchymal tissues within prostate capsules.

#207541 - $15.00 USD Received 4 Mar 2014; revised 1 Apr 2014; accepted 7 Apr 2014; published 14 Apr 2014

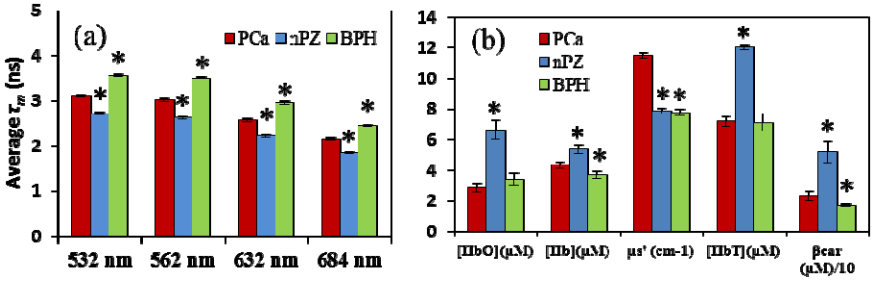

Fig. 4. (a) Comparison of four AFLS-derived mean-lifetimes, τ_m, at all four emission wavelengths across three tissue types (PCa, nPZ, and BPH). (b) Comparison of five LRS-derived features across the three tissue types. μ_s' was calculated at 750 nm, and β-car is scaled down by a factor of 10 for display purposes. For both (a) and (b), the symbol of '*' above bars indicates a statistically significant difference ($p < 0.05$) when compared to PCa. Error bars are based on standard error of mean.

In executing phase-one of data classification process (see Section 2.5) for AFLS only, the feature selection algorithm selected 15 out of 20 (i.e., 15/20) fitted AFLS parameters as an optimal feature set for 3-tissue-type classification, whereas 16/20 fitted AFLS parameters were selected for 5-tissue-type classification. For LRS only, all five parameters were selected by the feature selection algorithm for 'LRS only' classification and for both 3-tissue-type and 5-tissue-type classification. In case of dMOD, the selected feature number of parameters were 20/25 and 18/25 for 3-level and 5-level classification, respectively.

Table 2. Classification metrics of PCa for parenchymal tissues, evaluated by LRS only, AFLS only, and *dMOD* (unit: %)

Classification method	PCa Type	Mode	Sensitivity	Specificity	Accuracy	AUC*100
3-tissue-type classification*	All high grade (GS≥7)	*AFLS*	64.2 ± 2.5	69.2 ± 1.8	67.1 ± 0.7	72.9 ± 0.5
		LRS	63.0 ± 1.5	82.9 ± 1.6	74.7 ± 1.0	80.4 ± 0.2
		dMOD	79.0 ± 1.7	85.2 ± 1.1	**82.7 ± 0.7**	**90.8 ± 0.4**
5-tissue-type classification**	GS 9	*LRS*	84.4 ± 2.3	56.5 ± 0.7	59.4 ± 0.6	72.9 ± 0.5
		AFLS	76.5 ± 3.2	75.9 ± 1.0	76.0 ± 0.9	85.4 ± 0.6
		dMOD	82.3 ± 2.4	85.4 ± 0.7	**85.1 ± 0.6**	**91.5 ± 0.7**
	GS 8	*LRS*	71.8 ± 2.6	72.6 ± 1.8	72.5 ± 1.6	77.1 ± 0.7
		AFLS	76.3 ± 4.9	86.7 ± 0.8	86.0 ± 0.6	90.0 ± 0.6
		dMOD	81.5 ± 3.4	90.8 ± 0.9	**90.1 ± 0.8**	**93.6 ± 0.7**
	GS 7	*LRS*	71.9 ± 2.2	82.7 ± 1.3	80.2 ± 0.7	87.9 ± 0.2
		AFLS	70.9 ± 2.0	72.4 ± 0.9	72.1 ± 0.7	78.6 ± 0.7
		dMOD	86.0 ± 2.4	88.5 ± 0.7	**87.9 ± 0.6**	**94.7 ± 0.4**

* The values listed in this category implicate the classification for all high-grade PCa tissue group against non-cancer tissue types (nPZ and BPH). ** The values listed in this category implicate the classification for each PCa tissue group (e.g., GS 9) against remaining tissue groups. All are high grade (GS≥7).

#207541 - $15.00 USD Received 4 Mar 2014; revised 1 Apr 2014; accepted 7 Apr 2014; published 14 Apr 2014

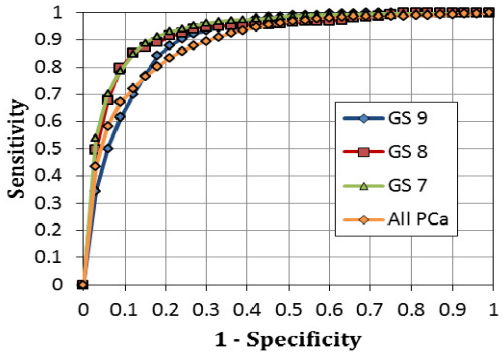

Fig. 5. ROC curves obtained using the *dMOD* and the MLR classification for identifying parenchymal PCa tissues at individual PCa grades (GS 9, GS 8, GS 7) using 5-tissue-type classification and with all grades combined (All PCa) using 3-tissue-type classification.

After generating the MLR classification models using selected features and completing phase-two data process for 3-tissue-type classification, we were able to evaluate classification accuracy by quantifying Sn, Sp, Acc, and AUC for all high-grade PCa (i.e., all GS≥7 combined) with classification based on AFLS and LRS, individually or combined, as listed in Table 2. It is clear that *dMOD* gives rise to the best sensitivity (79.0%), specificity (85.2%), accuracy (82.7%), and AUC (90.8%) for PCa classification compared to either of the two techniques (AFLS and LRS). Furthermore, we repeated phase-two data process for 5-tissue-type classification, and the analysis outcome was also excellent as shown in Table 2. The authors' two-phase classification method allows identification of PCa tissue at the individual Gleason grade, namely, GS = 7, 8, and 9, and to return the best classification performance by its sensitivity, specificity, accuracy and AUC for all three PCa grades. It is clear that *dMOD* is the optimal approach to be able to accurately classify not only PCa tissue but also its specific Gleason grade. Three corresponding ROC curves obtained by *dMOD* for respective Gleason scores are illustrated in Fig. 5. One extra ROC curve for all PCa grades combined, as determined by 3-tissue-type classification from *dMOD*, is also plotted in Fig. 5 for comparison. This figure reveals that the overall performance from 5-tissue-type classification is superior, particularly for PCa tissue with Gleason grades of GS=7 and GS=8 compared to 3-tissue-type classification.

3.2 Results from extra-capsular tissues on the gland capsules

For extra prostatic or extra capsular tissues (ECT), the measured AFLS/LRS data sets were taken from 185 small sites on or adjacent to the prostate capsules of additional eight patients. Analysis of means for AFLS data revealed that ECT lifetimes were closer to those of BPH and significantly longer than those from PCa. Also, in LRS, oxy- and total hemoglobin concentrations were significantly lower, whereas deoxy-hemoglobon concentration was significantly higher in PCa tissues than in benign ECT. In particular, light scattering of PCa at 750 nm was still significantly larger than that in benign ECT, which is very consistent with the case of parenchymal benign tissues (see Fig. 4).

#207541 - $15.00 USD Received 4 Mar 2014; revised 1 Apr 2014; accepted 7 Apr 2014; published 14 Apr 2014

Table 3. Classification metrics to discriminate PCa from benign tissues (including ECT), evaluated by LRS only, AFLS only, and *dMOD* (unit: %)

Classification method	PCa Type	*Mode*	Sensitivity	Specificity	Accuracy	AUC*100
3-tissue-type classification*	All high grade (GS>7)	*AFLS*	86.6 ± 1.7	79.4 ± 1.2	82.1 ± 0.8	92 ± 0
		LRS	76.7 ± 0.5	92.6 ± 0.7	86.6 ± 0.4	93 ± 0
		dMOD	92.1 ± 1.0	92.4 ± 0.8	**92.3 ± 0.5**	98 ± 0
5-tissue-type classification**	GS 9	*LRS*	80.2 ± 2.0	78.2 ± 0.5	78.4 ± 0.3	85 ± 1
		AFLS	88.1 ± 2.7	91.7 ± 0.2	91.4 ± 0.4	95 ± 1
		dMOD	82.8 ± 1.8	95.5 ± 0.5	**94.3 ± 0.5**	96 ± 1
	GS 8	*LRS*	70.3 ± 5.3	79.7 ± 0.8	79.1 ± 0.8	81 ± 0
		AFLS	76.8 ± 2.1	92.3 ± 0.3	91.3 ± 0.3	93 ± 1
		dMOD	83.5 ± 3.2	92.5 ± 0.3	**91.9 ± 0.3**	95 ± 1
	GS 7	*LRS*	87.1 ± 2.3	80.4 ± 1.0	81.8 ± 0.8	92 ± 0
		AFLS	83.3 ± 1.2	76.0 ± 0.9	77.5 ± 0.7	88 ± 0
		dMOD	91.4 ± 1.4	91.0 ± 0.3	**91.1 ± 0.3**	97 ± 0

We utilized the same multinomial classification with 10-fold cross validation to evaluate the accuracy of *dMOD* to discriminate PCa tissues from ECTs and nPZ. The feature sets for 3-tissue-type classification included 11 features out of 20 from AFLS, all 5 features from LRS, and 23 parameters from the dual-modal method. Also, the feature sets for 5-tissue-type classification included 16, 5, and 16 fitted parameters from AFLS, LRS, and *dMOD*, respectively, after executing the feature selection algorithm. The final outcome of phase two classification analysis for both 3-tissue-type and 5-tissue-type classification is listed in Table 3. The former classification gave rise to 92.3% accuracy when identifying any level of high grade PCa (GS>7) in the presence of benign ECTs and nPZ tissue; the latter classification resulted in a range of accuracy between 91.1% to 94.3% when identifying high grade PCa by Gleason scores in the presence of these benign tissues. In comparison, *dMOD* offered overall excellent performance and better classification accuracy than each modality alone (i.e., either LRS or AFLS), as clearly demonstrated in the Table.

It is also noted that when being stratified by Gleason grade, AFLS data provided high accuracy of ~91% for both GS 9 and GS 8, which is comparable to the accuracy obtained by *dMOD*. However, the accuracy for identifying PCa with GS 7 is much better by *dMOD* (91%) than by either AFLS (77.5%) or LRS (81.8%). The analysis results given in Table 3 confirm that *dMOD* can provide excellent accuracy in discriminating high grade PCa (with or without identifying Gleason scores) from benign parenchymal and extra capsular tissues. The corresponding ROC curves determined by both 3-tissue-type and 5-tissue-type classification methods with *dMOD* data are shown in Fig. 6. Being consistent with Table 3, this figure reveals that the overall performances of these two classification methods are comparable, giving rise to high accuracy, as long as *dMOD* is utilized for data analysis and classification. Both Table 3 and Fig. 6 support that *dMOD* has great potential to be developed as an excellent tool for positive margin assessment during or right after radical prostatectomy, thus improving the management and treatment outcomes of PCa.

#207541 - $15.00 USD Received 4 Mar 2014; revised 1 Apr 2014; accepted 7 Apr 2014; published 14 Apr 2014

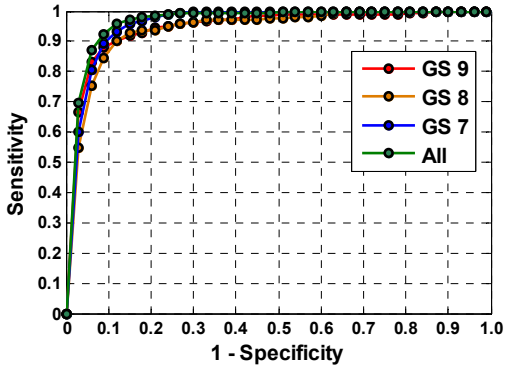

Fig. 6. ROC curves obtained using the *dMOD* and MLR classification for identifying PCa and ECTs at individual Gleason grades (GS 9, GS 8, GS 7) using 5-tissue-type classification and with all grades combined (All PCa) using 3-tissue-type classification.

4. Discussion and conclusions

Optical imaging and measurement techniques are increasingly being developed, evaluated, and/or utilized for a broad range of medical applications. Of particular interest is their potential to differentiate benign from malignant tissue with high sensitivity and specificity. In particular, successful application of optical imaging techniques may have the potential to significantly impact current treatment paradigms for prostate cancer among others, improving diagnostic yield of prostate biopsies, monitoring of PCa foci within the prostate during active surveillance, and assessing surgical margins during radical prostatectomy. For these specific reasons, we hypothesized in the present study that a dual-modality optical method using AFLS and LRS has the ability to detect and differentiate high grade PCa tissues from benign, low-risk ones. To prove this hypothesis, we integrated a *dMOD* system, measured *ex vivo* human prostate glands, implemented feature selection and classification algorithms, and investigated the capabilities of discriminating high grade PCa from benign prostate tissues based on fitted parameters from AFLS and LRS, individually and in combination. In this section, we will discuss data classification algorithms, compare *dMOD* system performance, and compare our approaches with published methods. We will also discuss biochemical and/or physiological mechanisms resulting in signal differences of AFLS/LRS induced by PCa. Finally, we will discuss limitations of our proposed classification method.

4.1 MLR classification models

Although several parameters in both LRS and AFLS exhibit significant differences between PCa and benign tissues, none of these parameters can be singly used to discriminate PCa from benign tissues. While these parameters are associated with anatomical or physiological or biochemical behaviors of the tissues, standard deviations of these parameters are quite high, which can be attributed to the heterogeneity of the tissues and insufficient intrinsic contrasts as well. The MLR algorithm was thus employed: first to identify critical features (using sequential feature selection [24]), followed by combining the selected features to create a decision model for identifying different tissue types (see Section 2.5).

Two different models were realized in this study: (1) 3-tissue-type classification for discriminating high grade PCa (GS≥7) from benign tissues, and (2) 5-tissue-type classification for discriminating PCa stratified by Gleason scores. While the ability to identify high grade PCa is important, the ability to detect PCa at GS = 7 is particularly more significant and clinically meaningful. This is because GS = 7 is the critical landmark of aggressive PCa and marks the action timeline from active surveillance to aggressive treatment in order to have early treatment with effective outcomes. Therefore, our 5-tissue-type

#207541 - $15.00 USD Received 4 Mar 2014; revised 1 Apr 2014; accepted 7 Apr 2014; published 14 Apr 2014

classification method for identifying PCa stratified by Gleason scores is potentially more useful for future clinical applications.

4.2 Performance of dMOD approach and comparison to published works

We hypothesized in the beginning of this study that LRS and AFLS, separately or in combination, could enable detection and identification of PCa tissue at high grades from either parenchymal tissues within prostate capsules or extra-prostatic tissues on or adjacent to the capsules. Our results proved that the *dMOD* approach, which combined LRS and AFLM for tissue classification analysis, gave rise to the highest accuracy for PCa tissue discrimination, in comparison to either technique alone for both intra-capsular as well as extra-capsular tissues.

When 3-tissue-type classification was performed on intra-prostatic tissues, our two-phase classification algorithm and ROC analysis showed that AFLS and LRS individually had discriminative accuracy of 67.1% and 74.7%, respectively. AFLS and LRS also had a similar sensitivity, but LRS had a higher specificity for detection of PCa without identifying cancer grade. When parameters from the two modalities were combined (*dMOD*), discriminative accuracy, sensitivity and specificity for PCa (all grades combined) were significantly improved (Table 2). Consistently, *dMOD* improved accuracy over those by the individual modalities for discriminating individual grades of PCa (GS = 7,8,9) with respect to the benign tissue (Table 2), when 5-tissue-type classification approach was performed. Similar conclusions were clearly held on extra-capsular data (Table 3), except that the classification accuracies from each of the two techniques were much higher than those in the intra-prostatic case. In fact, for GS of 8 and 9, AFLS results were almost comparable (though not as high) to *dMOD*, but Gleason 7 was significantly less accurate for AFLS alone.

Overall, it is clear from Tables 2 and 3 that classifying PCa stratified by Gleason scores considerably improved the classification accuracy in comparison with the all-grade-combined approach. This observation implies that PCa at different Gleason scores (i.e., at different aggressive levels) exhibits unique fluorescence and reflectance properties, which are closely associated with their respective biochemical and/or physiological mechanisms, which will be discussed in the next sub-section. This also makes the 5-tissue-type classification model be the method of choice for accurately identifying PCa.

While prior published reports on methods designed towards discriminating PCa tissues *in vivo* are limited, several optical studies using *ex vivo* prostate specimens have been found [13–15,20]. The study by Salomon et. al. [13] used a triple spectroscopy approach on frozen-then- thawed *ex vivo* prostate tissue (16 malignant and 75 benign samples) to discriminate malignant from benign tissue. Their technique involved spectral measurement and assessment from laser-induced auto-fluorescence, white-light remission, and high-frequency impedance spectroscopy. They reported a cross-validated sensitivity and specificity of 75% and 87.3%, respectively, which are comparable to our results. Halter et al. [20] measured electrical properties of 71 malignant and 465 benign *ex vivo* samples and reported a maximal accuracy of 81.8% for PCa tissues with GS≥ 7. In comparison, with *dMOD,* we obtained an accuracy of 82.7% for differentiation of PCa with GS≥ 7 (Table 2) in parenchymal tissues, showing equal or better accuracies of PCa detection compared to the two methods aforementioned. Furthermore, two other optical technologies with high or cellular spatial resolution, OCT [14] and CARS [15], were explored recently as a potential imaging tool to identify positive PCa margins and/or cavernous nerves for guiding radical prostatectomy. While OCT provided a high image resolution in depth up to 1 mm, it seemed to lack physiology-based specificity, resulting in a fairly good sensitivity (70%) and specificity (84), excellent negative predictive value (96%), but a poor positive predictive value (33%) [14]. Since CARS is a microscope-based facility, it is able to image PCa and cavernous nerves at a cellular resolution. The results shown in [15] confirmed that CARS has the potential to become a clinical tool for surgical-margins assessment for PCa, while no classification of PCa at any GS was reported.

#207541 - $15.00 USD Received 4 Mar 2014; revised 1 Apr 2014; accepted 7 Apr 2014; published 14 Apr 2014

4.3 Origin and significance of measured parameters

4.3.1 Fluorescence signals

It is well known that optical fluorescence is closely associated with biochemical components/compounds or metabolic status within tissues, so it has been utilized in the field of biomedical research for decades, with either intensity or lifetime measurements. Numerous reviews on this topic can be found in literature, and two examples are given in [26,27]. As we mentioned in our previous study [24], measurement of fluorescence lifetime provides much information on the mechanisms that lead to chemical or biochemical processes. Furthermore, each pair of excitation/emission (ex/em) light either matches or corresponds to a set of electron energy levels for a specific molecular structure or biochemical bond. It has been a common practice over the past few decades to select 350 nm/450 nm as the ex/em pair since this pair is directly linked to the oxidized form of nicotinamide adenine dinucleotide, which is a major electron acceptor. In its reduced form, it is called NADH. The reduced nicotinamide ring is ñuorescent, which enables investigators to gain insight into the redox state of tissue and cellular metabolism [26]. Many studies have shown that the fluorescence signals from NADH are often reduced in tumor tissues due to a decrease in relative amount of NADH in malignant tissues [26].

In this study, however, we did not utilize NADH as an endogenous tissue fluorophore to probe PCa. We selected λ_{ex} = 447 nm for several reasons: (1) to push the spectral window towards longer wavelengths than ultraviolet light in order to have a deeper light penetration depth, (2) to explore other biochemical components or processes that may be linked to PCa, and (3) to find other possible biomarkers (besides NADH) for high grade PCa detection. Throughout the study, our findings show that all fluorescence signals at λ_{em} = 532, 562, 632, and 684 nm have exhibited shorter lifetimes [see Fig. 4(a)] by PCa at all high grade levels (GS≥7) than by the benign peripheral zone (nPZ) tissues. The next question is: What biochemical molecules are probed at these four wavelengths, and how are they affected by or associated with PCa?

Based on existing literature on *in vivo* fluorescence spectroscopy [28] and fluorescence lifetime, we expect that our selected excitation at 447 nm targets such endogenous fluorophores as lipopigments, flavins, and porphyrins within the prostate tissues. According to [28], porphyrin emission becomes dominant only after 600 nm, flavins have an emission peak between 500 and 600 nm, and lipopigments have a strong and broad emission band around ~450-700 nm (centered at ~560 nm). This implies that our detected fluorescence signals result from a combination of more than one fluorophore: specifically, both flavins and lipopigments contribute the fluorescence signals at 532 nm and 562 nm, while both lipopigments and porphyrins influence the signals at 632 nm. Indeed, the lifetimes observed at the respective four wavelengths in this study match well with those of key biochemical compounds [27] within lipopigments, flavins, and porphyrins. The key point in the following is to discuss and understand why high grade PCa alternate fluorescence signals and lifetimes of lipopigments, flavins, and porphyrins.

First, one major chromophore within lipopigments is lipofuscin, which consists of yellow-brown-colored granules and is marked as one of the aging or “wear-and-tear” pigments. Lipofuscin can be considered as a later phase of the cellular digestion chain associated with lysosomes, which are cellular, enzyme-containing organelles and serve as the stomach of the cell to process waste materials and cellular fragments [29]. Many diseases, such as macular degeneration, Alzheimer's disease, and Parkinson's disease, have been reported to have abnormal accumulations of lipofuscin. Thus, we speculate that high grade PCa tissue is likely to have ill-behaving lysosomes, which are not able to perform well cellular disposal function and thus lead to unhealthy accumulation of lipofuscin within the prostate tissue. Next, it is well known that flavin adenine dinucleotide (FAD) is a redox cofactor, playing a key role in cellular metabolism. FAD often exists in two different redox states: the oxidized form, FAD,

#207541 - $15.00 USD Received 4 Mar 2014; revised 1 Apr 2014; accepted 7 Apr 2014; published 14 Apr 2014

and reduced form, $FADH_2$ [29]. The former is fluorescent, while the latter one is not. It is often seen that the fluorescence signals from FAD are largely reduced in tumor tissue because of the decrease in the oxidized form of flavins. Last, since porphyrins are a group of organic compounds, one of which is heme, the pigment in red blood cells and a cofactor of the protein hemoglobin, we expect to see alternations in porphyrins fluorescence signatures due to diseased vasculature of PCa tissues. Given all the biochemical relations between the measured fluorescence signals and PCa, we conclude that our AFLS signals enable us to probe PCa status due to damaged or defective functions in cellular disposal and metabolic processes as well as ruined blood vasculature. Table 4 summarizes the relations between the measured fluorescence signals and biochemical compounds that are altered in their functions by PCa. This table implies that it might be possible to identify specific changes in lifetime from each of the three biochemical compounds/fluorophores, so as to reveal cellular or metabolic alternations due to PCa, by decomposition of lifetime decay signals. However, it is beyond the scope of this paper and will be explored in our future studies.

Table 4. Summary of relations among fluorophores, cellular or metabolic functions, and expected versus measured fluorescence signals and lifetimes at emission wavelengths

Biochemical fluorophores in prostate tissue	Relations to cellular/metabolic functions of tissue	Fluorescence expected (spectral band; peaks) in nm [28]	Fluorescence measured [see Fig. 4(a)] (τ: lifetime in ns)		
			Peak	τ; cancer	τ; benign
Porphyrins	Tissue vasculature	> 600; 630, 680	632 nm 684 nm	2.59 ± 0.49 2.17 ± 0.40	2.22 ± 0.45 1.85 ± 0.32
Flavins	cellular metabolism	500-600; 550	532 nm 562 nm	3.12 ± 0.44 3.03 ± 0.48	2.72 ± 0.37 2.63 ± 0.38
Lipopigments	cellular disposal process	450-670; 560	532 nm 562 nm 632 nm	3.12 ± 0.44 3.03 ± 0.48 2.59 ± 0.49	2.72 ± 0.37 2.63 ± 0.38 2.22 ± 0.45

While NADH is an endogenous tissue fluorophore to probe metabolic states of tissue and/or cancer, we investigated three other biochemical and molecular signatures of prostate cancer using AFLM with excitation at 447 nm and emission at 532, 562, 632, and 684 nm. Given the results in our previous study on breast cancer [24], we expect that the AFLM methodology demonstrated here is highly likely to work for cancer detection and classification in other types of cancer. Note that since the excitation-emission spectral bands of lipopigments, flavins, and porphyrins are rather broad, appropriate wavelengths for both excitation and emission can be possibly chosen in efficient spectral ranges depending on available optical hardware and choices of researchers.

4.3.2 Reflectance signals

Origin of LRS signals has been well understood and described in the biomedical optics literature. Basically, both chromophore concentrations, such as HbO and Hb, and light scattering, which reflects cell sizes and densities, can be estimated quantitatively from direct LRS measurements [25]. Several reported studies have utilized LRS with small fiber geometry to investigate various tissue types and cancer [30,31]. The physiological significance of LRS-derived HbO, Hb, and other chromophoes is self-evident as they provide absolute values of respective chromophore concentrations. Also, quantification of light scattering is directly associated with cell size and density: the larger and denser the particles

#207541 - $15.00 USD Received 4 Mar 2014; revised 1 Apr 2014; accepted 7 Apr 2014; published 14 Apr 2014

(such as cellular nuclei and intra-cellular organelles) are, the larger the light scattering coefficients are.

Our results in Fig. 4(b) clearly show that HbO, Hb, and HbT are all more prevalent in tissues within the benign peripheral zone, indicating overall better or fuller blood perfusions in the benign parenchymal tissues than in the PCa regions. Lower HbT values for PCa are also consistent with our previous work, taken from a different data set [11]. Furthermore, Fig. 4(b) also demonstrates that oxygen saturation (SO_2 = [HbO]/[HbT]*100) was lowest in PCa (39.7%), as compared to nPZ (55.3%) and BPH (47.9%), indicating relative hypoxia in the PCa region, also consistent with our previous study [11]. β-carotene was also found to be a contrast parameter for intra-prostatic tissues.

Moreover, as evident from Fig. 4(b), the light scattering coefficient (at 750 nm) of PCa was much higher than that of all benign tissue types consistently, resulting from morphological alternation in cellular size and density of PCa tissue. Indeed, it is suggested that as the PCa grade of tissue increases from low to high, glandular epithelial cells will progress toward prostatic intraepithelial neoplasia (PIN) and then become adenocarcinoma [32] with increased hyperplastic epithelium or/and cellular tufts filling the glandular space [33]. In the meantime, it was recently hypothesized that progression of PIN triggers reactive stroma formation, which is likely cancer-promoting, coevolves with foci of adjacent carcinoma, and thus changes cellular architecture and composition in both glandular and stroma space [33]. All of these morphological changes are the physiological origin to cause increases in light scattering.

4.4 Limitations and future work

Despite the promising results shown above, a few limitations of our study warrant discussion. First, both AFLS and LRS readings were recorded from *ex vivo* tissues approximately one hour after the prostates were disconnected from any blood supply. Re-evaluation of our methodology under *in vivo* setting may yield different spectral outputs, particularly for the spectral signatures of HbO, Hb, and HbT, given *in vivo* hemodynamic perfusion conditions and complex biochemical microenvironments.

Second, our prostate specimen sample size was relatively small and limited to patients with high grade PCa at GS≥7. Since identification of PCa at GS = 7 is highly critical in order to decide whether any treatment is needed, it is of necessity that the developed methodology needs to have high sensitivity and specificity. As such, further parameterization to characterize lower grades of PCa (i.e., GS≤6) should be mandatory prior to future clinical applications.

Third, the number of features used for *dMOD* tissue classification seems to be large and thus may lead to an overfitting concern. Because of non-perfusion conditions in our *ex vivo* prostate specimens, currently collected readings of HbO, Hb, and HbT may have large deviations due to a variety of physiological insults or defects. We expect that further *in vivo* studies may provide us with improved physiological conditions for the prostate glands during data collections, which in turn will reduce the deviations of fitted parameters and thus lead to a smaller number of features needed for accurate PCa classification.

Finally, our spectral signatures of PCa were all obtained within the prostate capsules (i.e., parenchyma tissues). Prior to *in vivo* applications, AFLS and LRS characteristic spectra of positive margins on prostate capsules will need to be identified and included for updated classification analysis.

Overall, this study was to investigate whether there exists any optical signature to discriminate PCa from non-cancerous prostate tissue and what kinds of optical signatures of PCa at different stages have. Much further development is needed before extending this technique to *in vivo* human environment. But, this study demonstrates that the *dMOD* methodology can be developed for *ex vivo* detection of positive margins in the operating room

#207541 - $15.00 USD Received 4 Mar 2014; revised 1 Apr 2014; accepted 7 Apr 2014; published 14 Apr 2014

during or right after radical prostatectomy, thus improving the management and treatment outcomes of PCa.

4.5 Conclusions

This study has demonstrated that the *dMOD* approach, which combines auto-fluorescence and light reflectance spectroscopy, is able to discriminate PCa at Gleason grade 7 or higher from benign parenchymal tissue as well as from capsular or extra-prostatic tissue types of *ex vivo* prostate specimens with excellent classification sensitivity, specificity and accuracy. With further development and validation, the *dMOD* approach has the potential to be developed as an intraoperative aid for positive margin assessment during radical prostatectomy, a minimally invasive aid for active surveillance strategies, and a complementary/integrated tool for other clinical applications.

Appendix: Cross-validation [34]

Cross-validation is commonly used to validate a new classification model by assessing how accurate the classification results are when the model is tested with an independent data set [34]. In general, a classification model is developed using a given dataset of known data as the training dataset to serve as "ground truth". Then, another independent dataset of unknown data is utilized as the testing dataset in order to test the model. In reality, the number of actual datasets is sometimes limited, so the testing results are not statistically conclusive. To solve this problem, k-fold cross validation is often employed by randomly partitioning the original datasets into k equal size subsamples. Next, a single subsample is kept as a testing dataset, while the remaining $k - 1$ subsamples serve as training data. To be statistically meaningful, this cross-validation process is performed k times, with each of the k subsamples rotated once as the validation or testing data. In a special case, where the measurement sample size, n, is relatively small, leave-one-out cross-validation is commonly used. Then, the independent, testing dataset is just one measurement; cross-validation will become an n-fold operation where n is the number of measurements. Specifically, we used 10-fold cross-validation in this study [see Fig. 3], with multiple data points in each training and testing datasets. Another example is given in ref [35], where leave-one-participant-out cross-validation was used to test their predication algorithm.

Acknowledgments

The authors acknowledge support in part by the DoD Prostate Cancer Research Program (W81XWH-11-1-0232) and the National Institutes of Health (R01CA138662). The authors express sincere appreciation to ISS, Inc (Champaign, IL) for their persistent support and technical assistance over years of study. We also appreciate the assistance from Mr. Henry Tran who provided key literature search on the relationship between observed fluorescence signals and biochemical compounds of tissue as well as prostate cancer.